Safe Robotized Polishing of Plastic Optical Fibers for Plasmonic Sensors

Francesco Arcadio, Marco Costanzo, Giulio Luongo, Luigi Pellegrino, Nunzio Cennamo and Ciro Natale

Dipartimento di Ingegneria, Università degli Studi della Campania "Luigi Vanvitelli", Via Roma 29, Aversa, Italy

Keywords: Human-robot Collaboration, Workspace Monitoring, Compliance Control, Plasmonic Optical Fiber Biosensors.

Abstract: Plastic optical fibers (POFs) biosensors are getting widespread in a number of application fields owing to their low cost, high performance, and for their extreme flexibility in terms of detection ability of a large number of specific substances in different matrices. A specific category of such sensors are those based on the surface plasmon resonance (SPR) phenomenon, which can be made very specific by suitable integration with a biological or chemical molecular recognition element (MRE), specifically designed for binding with the desired substance (the analyte). Despite the flexibility of the SPR-POF sensors, their production is still difficult to automate on a large scale because of the special polishing process of the plastic optical fiber. Such a process is currently performed by a human trained operator who rubs the surface of a short fiber segment against a sandpaper sheet by following an 8-shaped path while exerting a specific force in the direction normal to the contact surface. The present paper proposes the adoption of a collaborative robot programmed to perform the same task based on the data acquired from the human operator. To ensure the safe use of the robotic cell by operators who share the same workspace of the robot, the system is endowed with a workspace monitoring system that ensures the polishing task execution while minimizing the possible occurrence of collisions with human operators by suitable exploiting the kinematic redundancy of the robot.

1 INTRODUCTION

Highly sensitive plasmonic POF probes, combined with specific molecular recognition elements (MREs), can be obtained by exploiting modified POFs to obtain the interaction with the analyzed medium directly. For instance, a D-Shaped region must be realized to deposit a metal nanofilm, useful to excite the SPR phenomenon in this sensing area. The SPR phenomenon is a label-free technique where MREs, coupled to a metal surface (usually gold nanofilms), selectively recognize and capture the substance of interest, producing a local change in the refractive index at the metal surface interface by changing the resonance condition. This sensing approach, based on SPR-POF probes combined with MREs, can be used in several applications, such as medical diagnostics, environmental monitoring, industry, food safety, and security (Cennamo et al., 2021). The authors have combined the same SPR-POF platforms with different kinds of MREs, such as antibodies, aptamers, and molecularly imprinted polymers (MIPs), by obtaining interesting detection ranges in many applications. The limit of this sensing approach is the production process of the POF platforms because it is based on a polishing step, currently handmade. This limit yields inefficient process control to realize very similar sensors or to change their performances; hence, this kind of sensor cannot be produced on an industrial scale.

Automation of such a production process might be performed through the design of specific polishing machines or through a flexible automation approach like the use of robots. In the former case, the rigidity of the automation solution might be characterized by a low return on investment, since the scale of the automation system highly depends on the actual market demand of the sensor, which is very difficult to forecast for a new product. Therefore, such a rigid solution might be risky, especially for a startup. This motivated the approach proposed in the paper, which explores the possibility to adopt a modern collaborative robot (cobot) that can safely work in a highly dynamic environment shared with human operators (Natale, 2019). Programming of cobots is usually done by hand guidance but in the application at hand the motion trajectory the robot has to follow is very specific and it can be easily programmed by resorting to a motion primitive (Siciliano et al., 2009). Furthermore, following the given trajectory is not enough to carry out the polishing task properly, but a suitable normal force should be exerted during the mo-

Arcadio, F., Costanzo, M., Luongo, G., Pellegrino, L., Cennamo, N. and Natale, C.
Safe Robotized Polishing of Plastic Optical Fibers for Plasmonic Sensors.
DOI: 10.5220/0011123100003271
In *Proceedings of the 19th International Conference on Informatics in Control, Automation and Robotics (ICINCO 2022)*, pages 361-368
ISBN: 978-989-758-585-2; ISSN: 2184-2809

tion to ensure a proper abrasion of the plastic fiber cladding. This requires a force/motion control algorithm (Villani, 2020) and the approach proposed in this paper is inspired to (Haddadin et al., 2009), which is specifically suitable for elastic joint manipulators. A relevant aspect of any force control robotic application is the specification of the desired force profile. This work followed the well-known programming by demonstration strategy (Calinon, 2018); a human operator performs the task which has to be repeated by the robot and the necessary data are acquired. In this case, the contact force profile is recorded and a Gaussian Mixture Model is learned and then used to generate the force profile to track with the force control loop. The robot control system is eventually completed with a safe reaction strategy to the presence of human operators close to the robot arm. The robot workspace is constantly monitored by a RGB-D camera which track the skeletons of all human operators inside the workspace. The skeleton data are then used to compute the minimum distance from the robot that is the basis for a virtual repulsive action on the robot elbow which pushes this far away from the human operator. As soon as the operator goes out the robot worksapce, the elbow is brought to its nominal configuration by an elastic torque.

The collaborative robotic cell has been tested for the production of 10 sensor platforms, which have then been tested by using several water-glycerin solutions with different refractive indices. The results in terms of sensitivity and full width at half maximum of the resonance curve of all sensors demonstrate that the robotized polishing process ensures the expected quality and relieves the human operator from a relevant physical burden.

2 PRODUCTION PROCEDURE OF THE SPR-POF SENSOR

Intrinsic POF plasmonic sensors, where the modified POF interacts with the analyzed medium directly, have been presented to exploit different approaches, such as making a D-shaped POF sensing region. More specifically, about ten years ago, Cennamo et al. have presented a very simple to realize, low-cost, and high sensitive SPR sensor in Plastic Optical Fibers (Cennamo et al., 2011). To realize this SPR-POF sensor are necessary only three steps. In the first step, the optical fiber is fixed in a resin block to remove the cladding and part of the core in order to realize a D-shaped POF sensing area. These polishing steps are handmade exploiting two different polishing papers: a 5 μm polishing paper and a 1 μm polishing

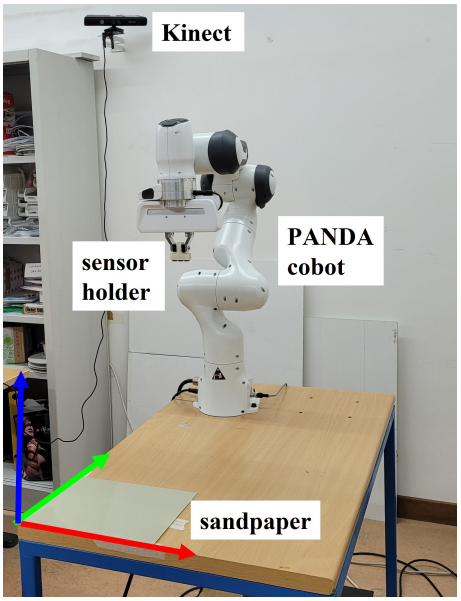

Figure 1: The collaborative robot for sensor polishing with the reference desk frame (RGB convention).

paper. The realized D-shaped sensing region is about 10 mm in length. In the second step, a thin buffer layer (e.g. a layer of Microposit S1813 photoresist), a layer with a refractive index major than the core of the POF, is deposited by a spin coater, to improve the interaction between the light and the plasmonic (SPR) phenomenon. Finally, in the third step, a gold nano-film (about 60 nanometers) is deposited by a sputter coater. The used POF has a PMMA core of 980 μm and a fluorinated polymer cladding of 10 μm (1,000 μm in total diameter). The experimental results reported in (Cennamo et al., 2011) have indicated that the configuration with the buffer layer exhibits better performance in terms of detectable refractive index range and of full width at half maximum of the SPR curve. In this work, sensor configurations without the buffer layer will be realized and tested. The buffer layer has been not used to test the automatic polishing process.

3 THE COLLABORATIVE CELL

This section describes the approach used to automate the polishing task of the SPR-POF sensor through the collaborative work cell shown in figure 1, in which a seven-joint robot and humans can work together. A Cartesian force/compliance control algorithm has been used to carry out the polishing task. A depth camera has been used to detect and avoid collisions with human operators in the robot workspace.

3.1 Perception System

The depth camera is a Microsoft Kinect v1 (see Figure 1). To correctly use the data provided by the camera in the robot control algorithm, it is necessary to perform the extrinsic calibration procedure aimed at determining the homogeneous transformation matrix $\boldsymbol{T}_c^b$ representing the pose of the camera frame with respect to the robot base frame. The following calibration procedure has been used:

1. A reference frame on the desk has been chosen as shown in Fig. 1.
2. Using an algorithm for the reconstruction of Point Cloud, the following three points have been identified: the origin of the desk frame, a point of the x axis and a point of the y axis of the desk frame. The three points were then used to compute the homogeneous transformation matrix $\boldsymbol{T}_{\text{desk}}^c$.
3. By positioning the robot through hand guidance and calculating the end-effector position through the direct kinematics, the following three points have been identified: the origin of the desk frame, a point of the x axis and a point of the y axis of the desk frame. The three points were then used to compute the homogeneous transformation matrix T_{desk}^b.
4. The homogeneous transformation matrix T_c^b is eventually computed as

$$\boldsymbol{T}_c^b = \boldsymbol{T}_{\text{desk}}^b \, (\boldsymbol{T}_{\text{desk}}^c)^{-1} \tag{1}$$

3.2 Skeleton Tracking

Realizing a safe Human Robot Collaboration (HRC) application requires a fast tracking algorithm which detects human operators in real time. For this purpose, the NiTE's skeleton tracking algorithm has been used. OpenNI/NiTE is a well known open-source framework that provides a set of APIs for body motion tracking that work with several perception systems, including the Microsoft Kinect v1 (PrimeSense, 2011). The algorithm tracks 15 joints for each operator in the scene in the form of a *skeleton* (see figure 2b) and returns the 3D position for each one of them: $\boldsymbol{s}_{i,k}^c$, $k = 1,2,\ldots,15$, $i = 0,\ldots,N$, being N the number of operators, that is 0 if no operator is detected in the scene. These positions are then used to compute the minimum distance d between a point on the robot elbow with position $\boldsymbol{p}_E^b$ and all human operators joints. Spheres were used to incorporate the untracked body portions and improve safety: a sphere with radius $r_1 = 0.14\,\text{m}$ was chosen for the head joint,

(a) Human operator close to the robot.

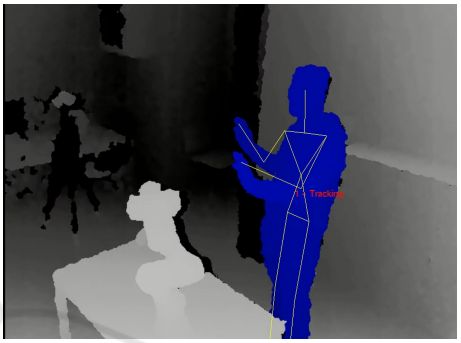

(b) Kinect depth view with the skeleton overlay.

Figure 2: The perception system for workspace monitoring.

a sphere with radius $r_E = 0.11\,\text{m}$ for the robot elbow and spheres with radius $r_j = 0.07\,\text{m}$ for the other joints of the skeletons. Once every captured joint position is expressed in the robot base frame through the homogeneous transformation matrix $\boldsymbol{T}_c^b$, the computation of d proceeds as follows

1. For each operator i in the scene, compute the minimum distance from the robot elbow and the human joints

$$d_i = \min_k \, d(\boldsymbol{p}_E^b, \boldsymbol{s}_{i,k}^b) \; i = 1,\ldots,N \tag{2}$$

where $d(\boldsymbol{p}_E^b, \boldsymbol{s}_{i,k}^b)$ is computed as

$$d(\boldsymbol{p}_E^b, \boldsymbol{s}_{i,k}^b) =$$

$$\begin{cases} \|\boldsymbol{p}_E^b - \boldsymbol{s}_{i,k}^b\| - (r_E + r_i) & \text{if } r_E + r_i \leq \|\boldsymbol{p}_E^b - \boldsymbol{s}_{i,k}^b\| \\ 0 & \text{otherwise} \end{cases}$$

2. Determine the minimum distance d as the smallest distance among the previously calculated ones

$$d = \min_i \, d_i \tag{3}$$

To correctly use the computed distance d in the control law of Section 3.3, the position $\boldsymbol{s}_{n,m}^b$ of the closest joint (m) of the closest operator (n) is stored.

3.3 Robot Control System

The torque control law proposed in this paper consists of three terms, i.e.,

$$\boldsymbol{\tau}(t) = \boldsymbol{\tau}_1(t) + \boldsymbol{\tau}_2(t) + \boldsymbol{\tau}_3(t). \tag{4}$$

The first term $\boldsymbol{\tau}_1(t)$ corresponds to the force/compliance control law, a hybrid force control scheme, which provides the robot with the capability to track a motion trajectory along the directions lying on the plane of the sandpaper while following a force profile in the orthogonal direction. In detail, the first control torque has been selected inspired by the passivity approach proposed in (Schindlbeck and Haddadin, 2015)

$$\boldsymbol{\tau}_1(t) = \boldsymbol{J}^T(\boldsymbol{q}(t)) \Big[\boldsymbol{K}_p \tilde{\boldsymbol{x}}(t) + \boldsymbol{K}_{p_f}(\boldsymbol{h}_d(t) - \boldsymbol{h}_e(t)) + \boldsymbol{K}_{i_f} \int_0^t (\boldsymbol{h}_d(\sigma) - \boldsymbol{h}_e(\sigma))\, d\sigma + \boldsymbol{K}_d \dot{\tilde{\boldsymbol{x}}}(t) \Big] \tag{5}$$

where $\tilde{\boldsymbol{x}}(t) = \boldsymbol{x}_d(t) - \boldsymbol{x}_e(t)$ is the pose tracking error, $\boldsymbol{K}_p \in \mathbb{R}^{6x6}$ and $\boldsymbol{K}_d \in \mathbb{R}^{6x6}$ are the position and damping gain positive definite diagonal matrices, $\boldsymbol{K}_{p_f} \in \mathbb{R}^{6x6}$ and $\boldsymbol{K}_{i_f} \in \mathbb{R}^{6x6}$ are diagonal positive definite matrices for the proportional and the integral control action on the force error, respectively, $\boldsymbol{J}(q)$ is the manipulator Jacobian, consistent with the chosen orientation representation, and $\boldsymbol{h}_d(t) = (\boldsymbol{f}_d^T(t)\ \boldsymbol{0}^T)^T$ and $\boldsymbol{h}_e(t) = (\boldsymbol{f}_e^T(t)\ \boldsymbol{\mu}_e^T(t))^T$ are the desired and the measured wrench vectors at the end effector, respectively. Note that, friction and gravity compensation terms are not reported since they are applied at low-level by the control interface of the robot.

The second term $\boldsymbol{\tau}_2(t)$ is designed to endow the collaborative robot with a collision avoidance behavior. Time dependence will be omitted for brevity. The term $\boldsymbol{\tau}_2$ consists of two contributions:

1. $\boldsymbol{\tau}_{2_{\text{rep}}}$. This term corresponds to a repulsive wrench $\boldsymbol{h}_r$, computed starting from the minimum distance d, so as to generate an internal motion that moves the elbow away from the operator. The repulsive wrench is defined as

$$\boldsymbol{h}_r = (\boldsymbol{f}_r^T\ \boldsymbol{0}^T)^T,$$

where $\boldsymbol{f}_r$ has been selected inspired by (Flacco et al., 2012) as follows

$$\boldsymbol{f}_r = \frac{F_{\max}}{1 + e^{\alpha\left(\frac{2}{\rho}d - 1\right)}} \boldsymbol{u} \tag{6}$$

where $F_{\max}$ is the maximum admissible magnitude, α is a shape factor, ρ represents the distance at which the magnitude of the repulsive force will approach zero and $\boldsymbol{u}$ is the unit vector along the direction defined by

$$\boldsymbol{u} = \frac{\boldsymbol{p}_E^b - \boldsymbol{s}_{n,m}^b}{\|\boldsymbol{p}_E^b - \boldsymbol{s}_{n,m}^b\|}$$

The torque $\boldsymbol{\tau}_{2_{\text{rep}}}$ is obtained by premultiplying the repulsive wrench by the transpose of the Jacobian $\boldsymbol{J}_4(q_1, q_2, q_3, q_4)$ of the manipulator consisting of the first 4 links only, i.e.,

$$\boldsymbol{\tau}_{2_{\text{rep}}} = \begin{pmatrix} \boldsymbol{J}_4^T(q_1, q_2, q_3, q_4) \\ \boldsymbol{O}_{3\times 6} \end{pmatrix} \boldsymbol{h}_r \tag{7}$$

2. $\boldsymbol{\tau}_{2_{\text{el}}}$. This term generates an elastic action so as to bring back the manipulator in the high-elbow configuration when no operator is in the workspace.

$$\boldsymbol{\tau}_{2_{\text{el}}} = \boldsymbol{K}_{\text{el}}(\boldsymbol{q}_{HE} - \boldsymbol{q}), \tag{8}$$

where $\boldsymbol{K}_{\text{el}} \in \mathbb{R}^{7x7}$ is the stiffness matrix, $\boldsymbol{q}_{HE}$ is a high-elbow configuration and $\boldsymbol{q}$ is the current configuration of the manipulator.

To ensure that the primary task is performed accurately even in the presence of an operator in the collaborative workspace, the repulsive and elastic torques have been projected into the null space of the transpose of the dynamically consistent pseudo-inverse of the Jacobian $\bar{\boldsymbol{J}}^T(\boldsymbol{q})$ (Khatib, 1987), i.e.,

$$\boldsymbol{\tau}_2 = \left(\boldsymbol{I} - \boldsymbol{J}^T(\boldsymbol{q})\bar{\boldsymbol{J}}^T(\boldsymbol{q})\right)\left(\boldsymbol{\tau}_{2_{\text{rep}}} + \boldsymbol{\tau}_{2_{\text{el}}}\right) \tag{9}$$

The third term $\boldsymbol{\tau}_3(t)$ is a compensation term, which ensures that the projected torque $\boldsymbol{\tau}_2(t)$ does not contribute to the end-effector acceleration, namely

$$\boldsymbol{\tau}_3 = -\boldsymbol{B}(\boldsymbol{q})\bar{\boldsymbol{J}}(\boldsymbol{q})\dot{\boldsymbol{J}}(\boldsymbol{q}, \dot{\boldsymbol{q}})\dot{\boldsymbol{q}} \tag{10}$$

4 LEARNING FROM THE HUMAN OPERATOR

The polishing task requires a long training phase of the human operator, not only in terms of the specific motion trajectory required to rub the optical fiber on the sandpaper, but also in terms of the normal force profile applied during the polishing. Therefore, we decided to transfer this skill from a trained human operator to the robot through a learning by demonstration approach (Calinon, 2018).

The first step of the learning from demonstration process is that of data acquisition. If it is well known that the motion trajectory to follow during the polishing process is a 8-shaped figure (Cennamo et al., 2011), no information on the most suitable normal force profile can be found in the literature. Thus, the actual force applied by a well-trained human operator

was acquired during a set of polishing trials through a 6D force sensor mounted on an handle suitably designed to keep the sensor platform hosting the POF in contact with the sandpaper.

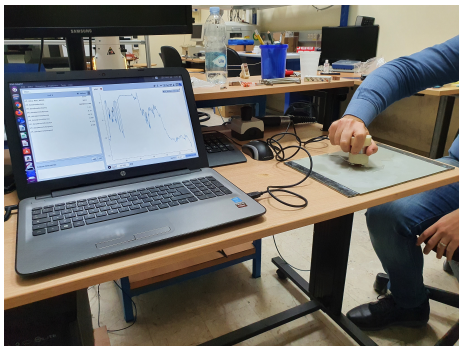

Figure 3: The human observation system.

The setup for the human observation depicted in Fig. 3 includes a Robotous RFT-40 force/torque sensor connected to a Ubuntu laptop via USB, so as to acquire the contact force along the normal to the surface at a rate of 200 Hz.

4.1 Contact Force Planning

The desired force profile $\boldsymbol{f}_d(t)$ used in the robot controller presented in Section 3.3 is generated by a Gaussian Mixture Regression (GMR), which was trained on the basis of the force data set acquired during four polishing trials, each 2 minutes long. In particular, the chosen Gaussian Mixture Model (GMM) of K Gaussian components (Calinon, 2018) is defined by the probability density function

$$p(\boldsymbol{\xi}) = \sum_{k=1}^{K} p(k)p(\boldsymbol{\xi}|k), \tag{11}$$

where $\boldsymbol{\xi}$ is the generic data point of the data set, $p(k)$ is the prior and $p(\boldsymbol{\xi}|k)$ is the conditional probability density function. A temporal regression problem for the normal force trajectory has to be solved, hence each data point is a couple $\boldsymbol{\xi} = (t\ f_z)^T \in \mathbb{R}^2$ and the parameters of the model are $\{p(k), \boldsymbol{\mu}_k, \boldsymbol{\Sigma}_k\}_{k=1}^K$, being

$$\boldsymbol{\mu}_k = \begin{pmatrix} \mu_{t_k} \\ \mu_{f_k} \end{pmatrix}, \quad \boldsymbol{\Sigma}_k = \begin{pmatrix} \sigma_{t_k} & \sigma_{tf_k} \\ \sigma_{tf_k} & \sigma_{f_k} \end{pmatrix} \tag{12}$$

the mean and the covariance matrix of the normal distribution of the kth component, respectively, i.e.,

$$p(\boldsymbol{\xi}|k) = \frac{1}{2\pi\sqrt{|\boldsymbol{\Sigma}_k|}} e^{-1/2(\boldsymbol{\xi}-\boldsymbol{\mu}_k)^T \boldsymbol{\Sigma}_k^{-1}(\boldsymbol{\xi}-\boldsymbol{\mu}_k)}. \tag{13}$$

These parameters can be estimated through the standard expectation maximization (EM) algorithm (Dempster et al., 1977). The method first requires an estimation of the number of components K and this can be carried out by training multiple models with different values of K and then selecting the value of K that optimize a given criterion. In this paper ten models have been estimated with $K = 1,\ldots,10$ and the Bayesian information criterion (BIC) has been adopted (Schwarz, 1978) to select the the optimal number of components $K = 2$.

Once the model has been trained, a GMR is used to generate the desired contact force profile $\boldsymbol{f}_d(t) = (0\ 0\ f_{z_d}(t))^T$ (Cohn et al., 1996), i.e.,

$$f_{z_d}(t) = \beta_1 \hat{f}_{z_1}(t) + \beta_2 \hat{f}_{z_2}(t) \tag{14}$$

$$\hat{\sigma}_f = \beta_1^2 \hat{\sigma}_{f_1} + \beta_2^2 \hat{\sigma}_{f_2} \tag{15}$$

where

$$\hat{f}_{z_k}(t) = \mu_{f_k} + \sigma_{ft,k}/\sigma_{t_k}(t - \mu_{t_k}) \tag{16}$$

$$\hat{\sigma}_{f_k} = \sigma_{f_k} - \sigma_{tf_k}^2/\sigma_{t_k} \tag{17}$$

are the conditional expectation and covariance of the desired force given the time t of each component. The two components are then weighted by the probability that the Gaussian component k has, being responsible for t, namely

$$\beta_k = \frac{p(t|k)}{p(t|1) + p(t|2)},\ k = 1,2. \tag{18}$$

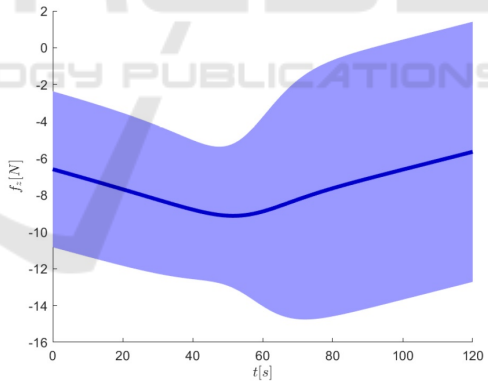

Figure 4: Result of the GMR retrival process.

Figure 4 reports the desired force profile generated by the GMR (14),(15), which has an average around -7 N but with a significant variance due to the large variability of the force exerted by the human operator in the different polishing trials despite his/her skill.

4.2 Motion Trajectory Planning

In order to execute the 8-shaped figure described in Section 2, the end-effector path has been defined according to a Lissajous figure, which is a curve lying

on a plane with parametric equation

$$\begin{aligned} x(t) &= A_x \sin(\omega_x t + \phi) \\ y(t) &= A_y \sin(\omega_y t + \phi) \end{aligned} \qquad t \in [0, 2\pi] \tag{19}$$

The shape of the curve is highly sensitive to the ratio ω_x/ω_y. In particular, the Lissajous figure that best suits the polishing task considered in this work is the one obtained with $\omega_x/\omega_y = 1/2$ that corresponds to a 8-shaped path. To allow the robot end effector follow the path described by the previous parametric equations, the desired end-effector position with respect to a frame f centered in the center of the Lissajous figure has to follow the path primitive

$$\boldsymbol{p}_d^f(s) = \begin{bmatrix} A_x \sin(\omega_x \frac{2\pi k}{L} s + \pi/2) \\ A_y \sin(\omega_y \frac{2\pi k}{L} s) \\ 0 \end{bmatrix} \quad s \in [0, L], \tag{20}$$

where L is the total path length (k times the length of a single Lissajous figure, being k the lap number). Denoting with $\boldsymbol{c}^b$ the position of the origin of the Lissajous figure and with $\boldsymbol{R}_f^b$ the rotation matrix representing the orientation of the Lissajous frame f with respect to the robot base frame, the end-effector planned position with respect to robot base frame is

$$\boldsymbol{p}_d^b(s) = \boldsymbol{c}^b + \boldsymbol{R}_f^b \boldsymbol{p}_d^f(s).$$

To obtain a desired end-effector position trajectory, a time law linked to the path described by the Lissajous figure is necessary. This can be accomplished by using a fifth-order polynomial with zero initial and final velocity and acceleration.

Finally, the desired orientation trajectory has to be specified, representing the end-effector orientation with the XYZ set of Euler angles. By making sure that at the beginning of the task the approach axis of the end-effector frame is orthogonal to the table, the desired orientation is set constant, i.e.,

$$\phi_d(t) = \phi_e(0) = \phi_0.$$

Moreover, in order to avoid the representation singularity (the pitch angle equal to $\pi/2$), the end-effector frame has been rotated of 180 deg about the y axis of the nominal end-effector frame so as to align the end-effector frame with the robot base frame, namely $\phi = \mathbf{0}$. Eventually, the desired end-effector pose used in the control law (5) is

$$\boldsymbol{x}_d(t) = \begin{bmatrix} \boldsymbol{p}_d^b(s(t)) \\ \phi_0 \end{bmatrix}, \quad \dot{\boldsymbol{x}}_d(t) = \begin{bmatrix} \dot{\boldsymbol{p}}_d^b(s(t)) \\ \mathbf{0} \end{bmatrix}. \tag{21}$$

5 EXPERIMENTAL VALIDATION

This section discusses the results obtained with the control law described in Section 3.3 in terms of performance of the robot and quality of the SPR-POF sensor obtained at the end of the polishing.

5.1 Testing of the Robot Controller

The following parameters have been selected for the control law described in Section 3.3

$$\boldsymbol{K}_p = \text{diag}\{2000,\ 2000,\ 650,\ 140,\ 140,\ 140\}$$
$$\boldsymbol{K}_{p_f} = \text{diag}\{0,\ 0,\ 0.5,\ 0,\ 0,\ 0\}$$
$$\boldsymbol{K}_d = \text{diag}\{100,\ 100,\ 650,\ \sqrt{50},\ \sqrt{50},\ \sqrt{50}\}$$
$$\boldsymbol{K}_{i_f} = \text{diag}\{0,\ 0,\ 1,\ 0,\ 0\},\ \boldsymbol{K}_{\text{el}} = 5.5\boldsymbol{I}$$

The proportional gain $\boldsymbol{K}_p$ along x and y directions has been chosen high enough to obtain a tracking error in the order of 1 cm, while along the z direction it has been chosen lower because along that direction the force control action should predominate. The damping gain $\boldsymbol{K}_d$ has been chosen so as to obtain a well-damped behaviour along all directions. The proportional $\boldsymbol{K}_{p_f}$ and integral $\boldsymbol{K}_{i_f}$ gains of the force controller have been tuned based on a linearized model of the system obtained considering an estimated contact stiffness of about 2600 N/m. Finally, the elastic gain $\boldsymbol{K}_{\text{el}}$ has been set as a trade off between the sensitivity to the virtual repulsive wrench $\boldsymbol{f}_r$ in (6) and the elastic torque that drives the elbow point towards the equilibrium configuration $\boldsymbol{q}_{HE}$ in (8).

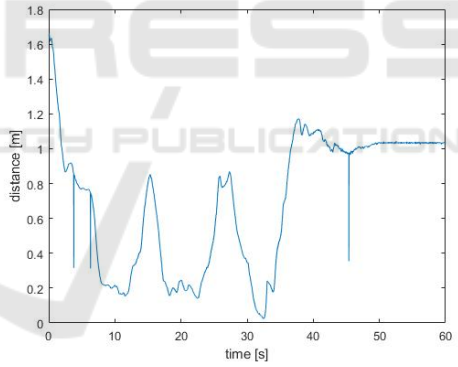

Figure 5: Minimum distance d during the experiment.

During the experiment a human operator has been trained to enter the robot workspace while the polishing task was being executed. The minimal distance d between the human operator and the robot elbow is reported in Fig. 5. Some spikes can be observed in the figure due to an occasionally wrong tracking of the skeleton by the Primesense algorithm. Nevertheless, their duration is negligible and they are filtered out by the torque controller, hence no corrections have been made.

Joint torque commands computed by the control algorithm in (4) allow the manipulator end-effector follow the Lissajous figure as reported in Fig. 6. Position and orientation errors are shown in Fig. 7.

During the polishing, the force $\boldsymbol{f}_e$ generated by the

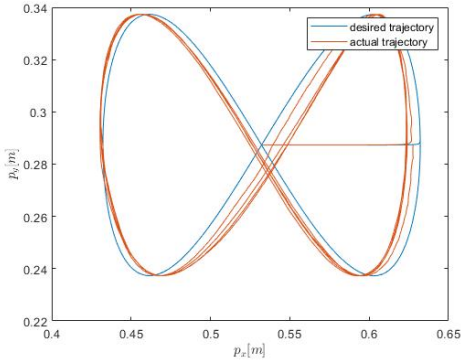

Figure 6: Desired and actual trajectories.

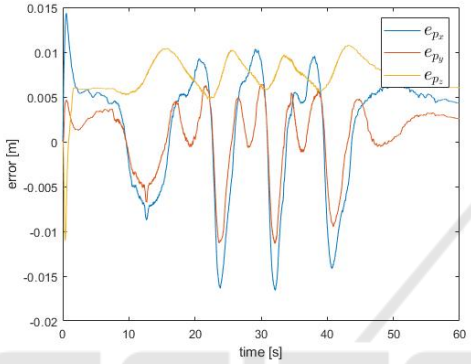

(a) Position tracking error.

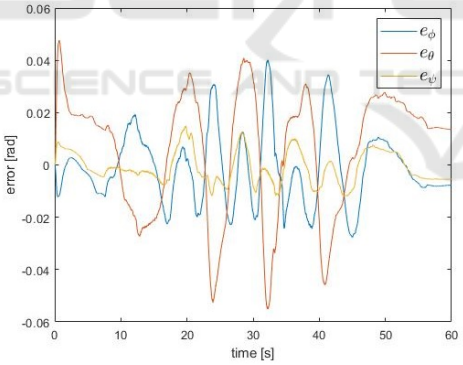

(b) Orientation tracking error.

Figure 7: Position and orientation tracking errors.

contact between the fiber and the sandpaper on the table is shown in Fig. 8. The x and y components are due to the friction necessary to carry out the polishing task successfully, hence they should not be counteracted, that is why proportional and integral gains along these directions are zero. The contact force has been estimated from joint torques and a dynamic model of the robot, according to the algorithm in (Magrini et al., 2014).

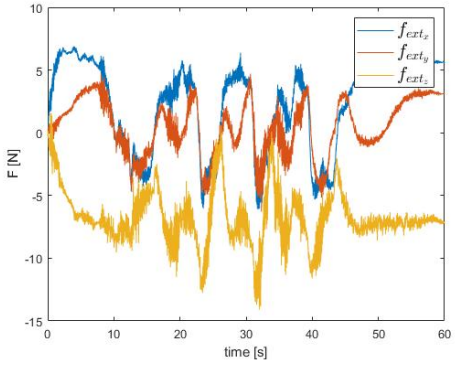

Figure 8: Force profile during motion.

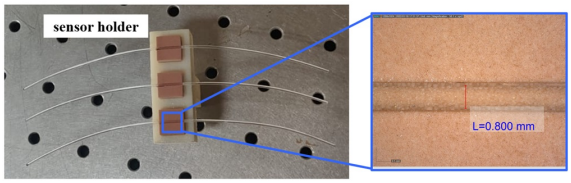

Figure 9: Top view of three POF sensor platforms at the end of the polishing task. The digital microscope view on the right shows the obtained length of the D-shaped fiber.

5.2 Sensor Production

Figure 9 shows the designed sensor holder, together with a view of the polished region, for one of the three sensors through a digital microscope. The D-shaped POF width of about 0.8 mm has been obtained through the automatic polishing process after one minute. It is worth emphasizing that the implemented automated procedure leads to noticeable time-saving. A reduction of about 70% can be achieved with respect to the handmade one. Note that the use of a robot for performing the polishing process allows to accurately control the depth of the D-shaped POF area and its roughness, by acting on the desired contact force and the speed of the motion trajectory. The depth parameter is particularly relevant for the sensor performance as it affects the quality factor of the plasmonic resonance (Gasior et al., 2014). After the automatic polishing process, a gold sputtering process has been used to realize the SPR-POF sensor.

5.3 Sensor Testing

Figure 10 reports the SPR transmission spectra obtained experimentally, normalized to the spectrum achieved with air as the surrounding medium, for several water-glycerin solutions with a refractive index ranging from 1.332 to 1.371. In particular, these results have been obtained exploiting a sensor configuration without a buffer layer. So, after the automatic

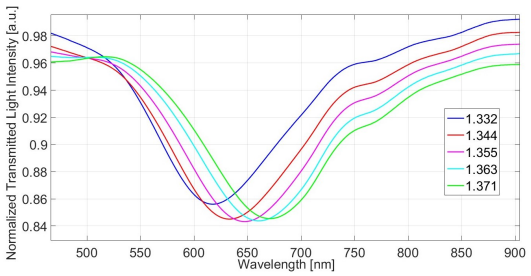

Figure 10: SPR spectra obtained by a D-shaped POF sensor without the buffer layer (with a gold nanofilm on the core of POF, directly) at different water-glycerin solutions in contact with the gold nanofilm.

polishing process here proposed, only a gold sputtering has been used to carry out the SPR-D-shaped POF sensor. We have characterized the SPR-POF sensor configuration without the buffer layer to better test the automatic polishing process here proposed. With respect to the SPR curves reported in (Cennamo et al., 2011) in the same configuration, the SPR curves here obtained present better performances in terms of full width at half maximum of the SPR curve, due to the automatic polishing process here proposed.

6 CONCLUSIONS

The experimental results presented in this paper demonstrate the feasibility of the proposed approach for automatic production of a SPR-POF sensor based on the human-robot collaboration paradigm. The robotized polishing phase results into a duration 70% shorter than the current handmade process. The quality of the polishing process is at least comparable to the handmade one as demonstrated by the SPR-POF sensor tests. A characterization of the actual roughness will be carried out by resorting to Atomic force microscope measurements. This will allow to optimize the process parameters. Moreover, the possibility to establish the contact force so as to obtain a given D-shaped depth with the aim to optimize the plasmonic resonant quality factor will be investigated.

ACKNOWLEDGEMENTS

This work was supported by the VALERE program of the University of Campania, CAMPANIA project.

REFERENCES

Calinon, S. (2018). *Learning from Demonstration (Programming by Demonstration)*, pages 1–8. Springer Berlin Heidelberg, Berlin, Heidelberg.

Cennamo, N., Massarotti, D., Conte, L., and Zeni, L. (2011). Low cost sensors based on spr in a plastic optical fiber for biosensor implementation. *Sensors (Basel)*, 11(12):11752–11760.

Cennamo, N., Pesavento, M., and Zeni, L. (2021). A review on simple and highly sensitive plastic optical fiber probes for bio-chemical sensing. *Sens. and Act. B: Chemical*, 331:129393.

Cohn, D., Ghahramani, Z., and Jordan, M. (1996). Active learning with statistical models. *J. Art. Intell. Res.*, 4:129–145.

Dempster, A., Laird, N., and Rubin, D. (1977). Maximum likelihood from incomplete data via the em algorithm. *J. Royal Statist. Soc.: Series B (Methodological)*, 29(1):1–38.

Flacco, F., Kroger, T., Luca, A. D., and Khatib, O. (2012). A depth space approach to human-robot collision avoidance. In *2012 IEEE Int. Conf. on Rob. and Aut.* IEEE.

Gasior, K., Martynkien, T., and Urbanczyk, W. (2014). Effect of constructional parameters on the performance of a surface plasmon resonance sensor based on a multimode polymer optical fiber. *Appl. Opt.*, 53(35):8167–8174.

Haddadin, S., Albu-Schaffer, A., Frommberger, M., Rossmann, J., and Hirzinger, G. (2009). The dlr crash report: towards a standard crash-testing protocol for robot safety - part II: Discussions. In *2009 IEEE Int. Conf. on Rob. and Aut.*, pages 280–287. IEEE.

Khatib, O. (1987). A unified approach for motion and force control of robot manipulators: The operational space formulation. *IEEE J. Rob. and Aut.*, 3(1):43–53.

Magrini, E., Flacco, F., and De Luca, A. (2014). Estimation of contact forces using a virtual force sensor. In *2014 IEEE/RSJ Int. Conf. on Intell. Rob. and Syst.*, pages 2126–2133.

Natale, C. (2019). *Physical Human-Robot Interaction*, pages 1–9. Springer London, London.

PrimeSense (2011). PrimeSense NITE Algorithms 1.5. https://www.yumpu.com/en/document/view/11580035/primesense-nite-algorithms-15-openni. Accessed on December 2021.

Schindlbeck, C. and Haddadin, S. (2015). Unified passivity-based cartesian force/impedance control for rigid and flexible joint robots via task-energy tanks. In *2015 IEEE Int. Conf. on Rob. and Aut. (ICRA)*, pages 440–447.

Schwarz, G. (1978). Estimating the dimension of a model. *Annals of Statistics*, 6(2):461–464.

Siciliano, B., Sciavicco, L., Villani, L., and Oriolo, G. (2009). *Robotics – Modelling, Planning and Control*. Springer.

Villani, L. (2020). *Hybrid Force and Position Control*, pages 1–6. Springer Berlin Heidelberg, Berlin, Heidelberg.